

THE COSMIC-RAY ELECTRON AND POSITRON SPECTRA MEASURED AT 1 AU DURING SOLAR MINIMUM ACTIVITY

M. BOEZIO, P. CARLSON, T. FRANCKE, AND N. WEBER
Royal Institute of Technology (KTH), S-104 05 Stockholm, Sweden

M. SUFFERT
Centre des Recherches Nucléaires, BP20, F-67037 Strasbourg-Cedex, France

M. HOF, W. MENN, AND M. SIMON
Universität Siegen, 57068 Siegen, Germany

S. A. STEPHENS
Tata Institute of Fundamental Research, Bombay 400 005, India

R. BELLOTTI, F. CAFAGNA, M. CASTELLANO, M. CIRCELLA, AND C. DE MARZO
Dipartimento di Fisica dell'Università and Sezione INFN di Bari, Via Amendola 173, I-70126 Bari, Italy

N. FINETTI, P. PAPINI, S. PICCARDI, AND P. SPILLANTINI
Dipartimento di Fisica dell'Università and Sezione INFN di Firenze, Largo Enrico Fermi 2, I-50125 Firenze, Italy

M. RICCI
Laboratori Nazionali INFN, Via Enrico Fermi 40, CP 13, I-00044 Frascati, Italy

M. CASOLINO, M. P. DE PASCALE, A. MORSELLI, P. PICOZZA, AND R. SPARVOLI
Dipartimento di Fisica dell'Università and Sezione INFN di Roma, Tor Vergata, Via della Ricerca Scientifica 1, I-00133 Roma, Italy

G. BARBIELLINI, U. BRAVAR, P. SCHIAVON, A. VACCHI, AND N. ZAMPA
Dipartimento di Fisica dell'Università and Sezione INFN di Trieste, Via A. Valerio 2, I-34147 Trieste, Italy

C. GRIMANI
Dipartimento di Fisica dell'Università di Urbino, I-61029 Urbino, Italy

J. W. MITCHELL, J. F. ORMES, AND R. E. STREITMATTER
Code 661, NASA/Goddard Space Flight Center, Greenbelt, MD 20771

AND

R. L. GOLDEN¹ AND S. J. STOCHAJ
Box 3-PAL, New Mexico State University, Las Cruces, NM 88003; stochaj@nmsu.edu
Received 1999 May 7; accepted 1999 October 26

ABSTRACT

We report on a new measurement of the cosmic-ray electron and positron spectra. The data were collected by the balloon-borne experiment CAPRICE94, which was flown from Lynn Lake, Canada, on 1994 August 8–9 at an altitude corresponding to 3.9 g cm^{-2} of average residual atmosphere. The experiment used the NMSU-WIZARD/CAPRICE94 balloon-borne magnet spectrometer equipped with a solid radiator Ring Imaging Cerenkov (RICH) detector, a time-of-flight system, a tracking device consisting of drift chambers and multiwire proportional chambers, and a silicon-tungsten calorimeter. This was the first time a RICH detector was used together with an imaging calorimeter in a balloon-borne experiment. A total of 3211 electrons, with a rigidity at the spectrometer between 0.3 and 30 GV, and 734 positrons, between 0.3 and 10 GV, were identified with small backgrounds from other particles. The absolute energy spectra were determined in the energy region at the top of the atmosphere between 0.46 and 43.6 GeV for electrons and between 0.46 and 14.6 GeV for positrons. We found that the observed positron spectrum and the positron fraction are consistent with a pure secondary origin. A comparison of the theoretically predicted interstellar spectrum of electrons shows that the injection spectrum of primary electrons is steeper than that of the nucleonic components of cosmic rays. Furthermore, the observed electron and positron spectra can be reproduced from the interstellar spectra by a spherically symmetric model for solar modulation; hence, the modulation is independent of the sign of the particle charge.

Subject headings: balloons — cosmic rays — elementary particles — Sun: activity

1. INTRODUCTION

Electrons and positrons together constitute about 1% of the total cosmic-ray flux. While rare, these components are important because their propagation through the Galaxy is governed by energy-loss processes different from those of cosmic-ray nuclei of the same energy. Because of their small

mass, electrons undergo severe energy loss caused by synchrotron radiation in the Galactic magnetic field, bremsstrahlung losses through interactions with the interstellar gas, and inverse Compton scattering with the ambient photons. Therefore, measurements of cosmic-ray electrons provide additional information about the physical conditions and the propagation of cosmic rays in the interstellar space not accessible from the study of cosmic-ray nuclear components.

¹ Deceased.

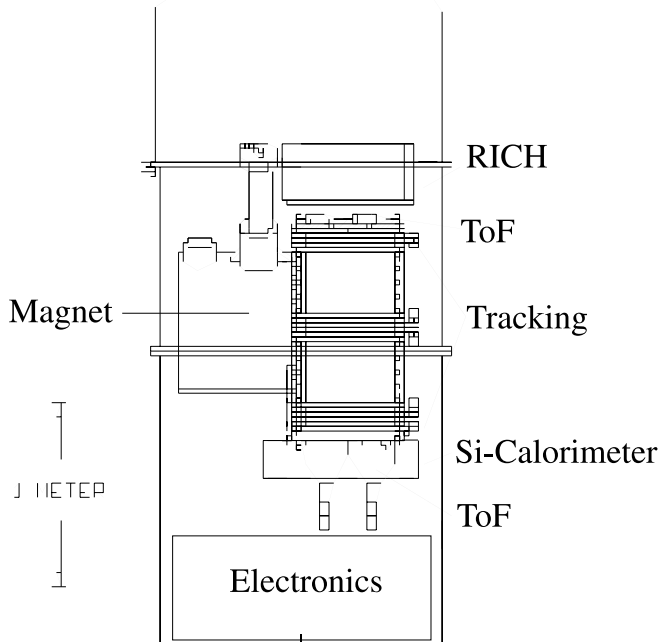


FIG. 1.—Schematic view of the CAPRICE94 apparatus

The observed cosmic-ray electrons and positrons may consist of a mixture of primaries accelerated in cosmic-ray sources, such as supernova remnants, and secondaries produced mainly by the interactions of cosmic-ray nuclei with the interstellar gas. In the latter case, they are the end product of the decay of short-lived particles (mostly pions via the decay $\pi^\pm \rightarrow \mu^\pm \rightarrow e^\pm$) produced in interactions, and a slight excess of positrons is expected over electrons. However, the observed positron fraction $e^+/(e^+ + e^-)$ at the top of the atmosphere (e.g., see Golden et al. 1996) is $\sim 10\%$ at a few GeV. Hence, a large majority of the electrons have to be of primary origin. If positrons are only, or mainly, of secondary origin, the positron spectrum provides a valuable test of the propagation models at energies where the energy-loss processes become important. This becomes possible because their production spectrum in the interstellar space could be calculated accurately, leaving the ambiguity of not knowing the exact shape of the accelerated spectrum in cosmic-ray sources.

In addition, precise measurements of the electron and positron spectra over a wide range of energy could be used to obtain information on the charge sign dependence of solar modulation and to determine the absolute modulation using the positron spectrum. The latter could be used to derive the interstellar spectra of electrons and other nuclear components.

Since the first unambiguous detection of electrons during the early sixties (Earl 1961; Meyer & Vogt 1961), a large number of experiments were performed using balloon-borne experiments. However, these measurements have produced results where the flux differ as much as a factor of 3 (e.g., see Golden et al. 1984). This is not very surprising considering the difficulty in identifying and measuring the energy of electrons in these first-generation experiments. With the recent advancement in the detector technology, more sophisticated experiments, each comprising many detector systems, have been performed. This approach pro-

vides a good control of the detector systems and the ability to determine accurately the detector efficiencies, their energy dependence, and the possible variation during the period of observation.

On the other hand, since the first detection of positrons in cosmic radiation in the sixties by De Shong, Hildebrand, & Meyer (1964) using a magnet spectrometer and by Daniel & Stephens (1965) by the use of arrival directions in the geomagnetic field, few attempts have been made over the past three decades. This is because of the difficulty in uniquely identifying positrons against the vast background of proton interactions in the detector and correcting for the positrons produced in the overlying atmosphere, which becomes increasingly important for energies below about a giga-electron volt. A few measurements (see Muller & Tang 1987 and references therein) reported an increase of the positron fraction, $e^+/(e^+ + e^-)$, for an energy above 10 GeV. A number of attempts were made to understand this anomalous increase theoretically and to confirm this finding experimentally. The later observations (Barwick et al. 1995; Golden et al. 1996) indicate that the positron fraction does not increase at high energy. It may be pointed out that while most of the recent measurements on the electron-positron component have been carried out above 5 GeV, only a few experiments attempted to obtain results below this energy (Barbiellini et al. 1996b; Clem et al. 1996; Barwick et al. 1997).

This paper reports results on observations of electron and positrons measured with the CAPRICE 1994 balloon-borne experiment. The apparatus was launched from Lynn Lake, Manitoba, Canada ($56^\circ 5'$ latitude north, $101^\circ 0'$ longitude west) on 1994 August 8 and it reached Peace River, Alberta, Canada ($56^\circ 15'$ latitude north, $117^\circ 2'$ longitude west). The balloon floated at an atmospheric pressure of 3.2–4.5 mbar (altitude of 36.0–38.1 km) for nearly 23 hr. This experiment used the NMSU-WIZARD/CAPRICE94 balloon-borne instrument consisting of, from top to bottom (Fig. 1), a Ring Imaging Cerenkov (RICH) detector, a time-of-flight (ToF) system, a superconducting magnet spectrometer equipped with multiwire proportional chambers (MWPC) and drift chambers (DC), and a silicon-tungsten imaging calorimeter. The combination of these independent detectors allowed for a rejection factor of better than 10^5 for protons against positrons and the ability to determine precisely all efficiencies. Furthermore, the unique properties of these detectors allowed us to measure a variety of cosmic-ray particles, which provided essential cross-checks of the results. Spectra of antiprotons, hydrogen and helium nuclei, and muons at various atmospheric depths have been obtained already and presented elsewhere (Boezio et al. 1997; Finetti 1998; Piccardi 1998; Boezio 1998²; Boezio et al. 1999a, 1999b).

Preliminary results on the positron fraction from the CAPRICE94 experiment were reported earlier (Barbiellini et al. 1996b). Here, we present the absolute energy spectrum of electrons in the energy region at the top of the atmosphere between 0.46 and 43.6 GeV and that of positrons between 0.46 and 14.6 GeV. We also describe in detail the analysis of the flight data. The detector system is described in § 2, the data analysis in § 3, and the results are presented and discussed in § 4.

² M. Boezio's thesis is also available at http://www.particle.kth.se/group_docs/astro/research/paper/mirko_thesis.ps.

2. DETECTOR SYSTEM

2.1. *The Ring Imaging Cerenkov Detector*

The Ring Imaging Cerenkov (RICH) detector of area $51.2 \times 51.2 \text{ cm}^2$ was designed primarily to identify anti-protons in the cosmic rays in a large background of electrons, muons, and pions (Carlson et al. 1994). The RICH used a 1 cm thick, solid sodium fluoride (NaF) radiator with a threshold Lorentz factor of 1.5 and a photosensitive multiwire proportional chamber with pad readout to detect the Cerenkov light image.

When a charged particle with velocity above the RICH threshold traversed the NaF radiator, Cerenkov light was emitted. The Cerenkov light refracted out of the crystal, and the cone of light expanded in a drift volume filled with nitrogen before it entered the photosensitive part of the detector through a quartz window. The Cerenkov photons were then converted into photoelectrons in the ethane-filled photosensitive volume containing 0.7% of the organic photoconverter compound tetrakis-(dimeylamino)-ethylene, also known as TMAE. The photoelectrons were amplified around the anode wires (128 wires of $15 \mu\text{m}$ diameter, separated by 4 mm) and they induced pulses on the wires as well as on the cathode planes.

The lower cathode plane was divided into 4096 squares of area $8 \times 8 \text{ mm}^2$, called pads, and the signals in both the pads and the anode wires were recorded. The RICH detector was enclosed in a box made of a strong frame of aluminum, covered with two 5 mm thick carbon fiber covers, which minimized the amount of material along the trajectory of the particle.

2.2. *The Time-of-Flight System*

The time-of-flight system consisted of two layers of plastic scintillators, one placed above the tracking system and the other below, as indicated in Figure 1. Each layer was divided into two paddles with a size of $25 \times 50 \text{ cm}^2$ and a thickness of 1 cm. The material used was Bicron 401. Each paddle had two 5 cm diameter photomultiplier tubes, one at each end. The distance between the two scintillator layers was 1.1 m.

The signal from each photomultiplier was split in two parts; one was sent to an analog-to-digital converter (ADC) and the other to a time-to-digital converter (TDC). In this way, the time-of-flight system provided both energy loss and timing information. The scintillator signals also were used to provide a trigger for the data acquisition system. The trigger was a fourfold coincidence between two photomultiplier tubes with signals in the top and bottom scintillator paddles, respectively. The threshold of each photomultiplier tube was set high enough to eliminate noise but low enough to provide an efficiency of nearly 100% to trigger minimum ionizing particles.

2.3. *The Superconducting Magnet Spectrometer*

The spectrometer consisted of a superconducting magnet, multiwire proportional chambers, and drift chambers.

The magnet (Golden et al. 1978) consisted of a single coil of 11 161 turns of copper-clad NbTi wire. The outer diameter of the coil was 61 cm and the inner diameter 36 cm. The coil was placed in a dewar filled with liquid helium surrounded by a vacuum shell close to a second dewar filled with liquid nitrogen that reduced the evaporation of liquid helium and enabled the attainment of a lifetime of 100 hr for

the superconducting magnet. The operating current was set at 120 A, producing an inhomogeneous field of approximately 4 T at the center of the coil.

The tracking system of CAPRICE94 consisted of a combination of two drift chambers (Hof et al. 1994) and eight multiwire proportional chambers (Golden et al. 1991). The MWPC had an active area of $45 \times 45 \text{ cm}^2$. The entrance windows of the chambers were made of mylar film of overall thickness 0.5 mm. All eight MWPCs could make position measurements in the bending direction (x) and four of them could also make measurements in the nonbending direction (y). The MWPCs were separated into three sets and located above, between, and below the drift chambers, as indicated in Figure 1. Typical resolutions ranged from 200 to $370 \mu\text{m}$ in the x -direction and from 840 to $960 \mu\text{m}$ in the y -direction.

The two drift chambers used for the trajectory measurements were physically identical. The lateral sides of the chamber box were made from 1 cm thick epoxy-composite plates, while the open top and bottom sides were covered with $160 \mu\text{m}$ thick copperplated mylar windows. The inner gas volume of the box was of size $47 \times 47 \times 35 \text{ cm}^3$. The drift chamber had six layers, with each layer containing sixteen 27.02 mm wide drift cells for measurements in the x -directions and four layers for the y -direction. The drift cells were arranged in double layers that were shifted by half a cell to solve the left-right ambiguity with respect to the sense wire (Hof et al. 1994). In a drift cell, the electrons liberated by the passage of an ionizing particle drifted to the anode wire under the effect of an applied electric field. The drift time of the electrons is related to the position at which the incident particle passed through the cell. This relation was obtained directly from the experimental data with an iterative least-squares fitting technique of the tracks (see Hof et al. 1994). A high efficiency ($\approx 99\%$ for a single drift cell) and a spatial resolution better than $100 \mu\text{m}$ were found over most of the range of possible drift paths.

2.4. *The Calorimeter*

The silicon tungsten calorimeter (Bocciolini et al. 1996) was an upgraded version of the calorimeter in the TS93 experiment that was flown in 1993 (Aversa et al. 1995). The calorimeter was designed to distinguish between minimum ionizing particles and hadronic and electromagnetic showers.

The calorimeter consisted of eight $48 \times 48 \text{ cm}^2$ silicon planes interleaved with layers of tungsten converter, each one radiation length (X_0) thick. A single plane consisted of an array of an 8×8 pair of silicon detectors mounted on a G10 motherboard. Each detector had a total area of $60 \times 60 \text{ mm}^2$ and was divided into 16 strips, each of width 3.6 mm. The detectors were mounted back-to-back with perpendicular strips to give x and y readouts. The strips of each detector were daisy-chained longitudinally to form one single strip 48 cm long. Taking into account all the material, the calorimeter had a total thickness of $7.2 X_0$ and 0.33 nuclear interaction lengths.

The segmentation of the silicon planes into strips provided information on the longitudinal and lateral profiles of the interactions along with the total deposited energy.

3. DATA ANALYSIS

The analysis was based on 60,520 s of data taken over a total acquisition time of 18 hr under an average residual atmosphere of 3.9 g cm^{-2} .

The CAPRICE94 instrument was well suited to identify electrons and positrons in the cosmic radiation. The tracking system reliably determined the charge sign and deflection over a wide rigidity range from 100 MV to 100 GV. The scintillators selected with high accuracy $|Z| = 1$ particles. With the combined capabilities of the RICH and calorimeter along with the time-of-flight information, electrons were identified against a background of muons and pions, and positrons were identified against a vast background of protons, muons, and pions. A rejection factor of better than 10^5 was achieved for protons against positrons. Furthermore, the capability of distinguishing different particles independently with the different CAPRICE94 detectors permitted the reliable determination of the rigidity-dependent efficiency and rejection power of each individual detector. This capability is unique to the CAPRICE experiments.

Electrons were selected in the rigidity interval in the spectrometer from 0.3 to 30 GV and positrons in the interval from 0.3 to 10 GV. The lower limit was owing to the geomagnetic cutoff. The nominal geomagnetic cutoff (Shea & Smart 1983) for the CAPRICE94 flight varied from ≈ 0.35 GV at Lynn Lake to ≈ 0.65 GV at Peace River. The upper limit for electrons was caused by statistics, while for positrons it was because of proton contamination. Above 5 GV, the RICH was not capable of separating protons from positrons; hence, protons contaminated the positron sample. However, up to 10 GV, the calorimeter selection permitted identification of positrons with a proton contamination of less than 30%.

3.1. Electron and Positron Selection

3.1.1. Tracking

The physically significant parameter measured by the spectrometer was the rigidity of the incident particle. This quantity, together with the trajectory of the particle in the spectrometer, was reconstructed by fitting the measured positions in the tracking system with an iterative least-squares procedure (see Golden et al. 1991 for a description of the track fitting process). For this work, the trajectory was determined by fitting only the information from the drift chambers. This made it possible to use the MWPC system for the efficiency estimation of the drift chambers (see § 3.3.1).

The conditions imposed on the fitted tracks for obtaining a reliable track reconstruction were:

1. At least nine (of 12) position measurements should be in the bending x -direction and five (of eight) in the non-bending y -direction.
2. There should be an acceptable χ^2 for the fitted track.
3. The estimated error on the deflection should be less than 0.04 (GV) $^{-1}$.

These criteria were based, in part, on the experience gained during the analyses of previous balloon flight experiments using the same magnetic spectrometer (see, e.g., Mitchell et al. 1996).

The resulting average maximum detectable rigidity was 150 GV. Hence, spillover was not a problem in this work since the upper rigidity limit was 30 GV.

3.1.2. Scintillators and Time of Flight

The scintillator system provided two sets of information: a measurement of the time of flight of the particle and two

measurements of the energy loss by ionization in the upper and lower scintillators. This information was used to first select downward moving particles. The time-of-flight resolution of better than 280 ps over a flight path of 1.1 m assured that no contamination from albedo particles remained in the selected sample. Second, it was used to reject heavier particles and multiparticle events. This selection rejected alphas and heavier particles, low-energy protons, and multiparticle events coming from interactions above the top scintillator. The interactions could take place either in the dome, the RICH, or in the top scintillators. Furthermore, there were showers induced in the gondola and balloon structure above the payload. For this selection, the following two conditions were applied to the data.

1. dE/dx losses in the top scintillator had to be less than 1.8 mip (most probable energy loss for a minimum ionizing particle).
2. Only one of the two top scintillator paddles should be hit.

Electron showers could produce backscattered photons and electrons in the calorimeter that could give an additional signal in the bottom scintillators. Also bremsstrahlung photons, produced above the spectrometer, could materialize in the bottom scintillators. None of these cases affected the tracking measurement or the calorimeter identification. Therefore, no restrictions were put on the bottom scintillators.

3.1.3. RICH

The RICH was used to measure the Cerenkov angle of the particle and thereby its velocity. The Cerenkov angle was reconstructed from the geometrical distribution of the signals in the pad plane (for a description of the reconstruction method, see Weber 1997).³ To use the RICH information correctly, the following set of conditions was applied to the RICH data (Boezio 1998).

1. A good agreement between the particle impact position as determined by the RICH and the tracking system was required. The difference in x and y should be less than three standard deviations, which was rigidity dependent but typically less than 5 mm.
2. Only events with one cluster of pads with high signals, typical of ionization from a charged particle, were accepted.
3. More than 3.5 pads were required in the fit for rigidities above 0.5 GV. Between 0.3 and 0.5 GV, at least 7 pads were required in the fit.
4. The reconstructed Cerenkov angle should not differ by more than three standard deviations from the expected Cerenkov angle for $\beta \approx 1$ particles.

The tracking information was used to obtain the direction of the incoming particle in the NaF crystals, and with this information, criterion 1 eliminated events that scattered in the RICH electronics. Criterion 2 eliminated multiple-charged tracks crossing the RICH. Criteria 3 and 4 were used to separate $\beta \approx 1$ particles from slower particles. The condition on the number of pads used in the fit was a compromise between rejection power and efficiency of the selection, and this was studied from flight data by selecting electrons and protons using the calorimeter. The number of

³ N. Weber's thesis is also available at http://msia02.msi.se/group_docs/astro/research/paper/niclas_thesis.ps.

pads required in the fit was higher below 0.5 GV to strengthen the electron identification in a rigidity region where the most worrisome contamination was caused by muons and pions. Protons were clearly separated from electrons in this rigidity region using dE/dx measurements as well as information from the calorimeter, as protons below 380 MV do not have enough energy to cross the plexiglass cover of the calorimeter and give a signal only in the first silicon layer.

Figure 2 shows the measured Cerenkov angle for events selected with RICH criteria 1, 2, and 3. The bands corresponding to $\beta \approx 1$ (electrons, muons, and pions), protons, deuterons, and ^4He can be identified. The solid lines indicate the electron selection region based on the Cerenkov angle. However, it is important to point out that the solid lines in the figure are just approximations of the real selection. The RICH selection was done on an event-by-event basis. For each event, the Cerenkov angle and the corresponding resolution were obtained, the latter depending on the incidence angle of the particle (see Barbiellini et al. 1996a). The distribution of the Cerenkov angle for protons starts to overlap with the $\beta \approx 1$ particles above 3 GV. Above 5 GV, no separation against protons was possible and the RICH criteria were not applied. Note that the RICH also rejected deuterons and heavier particles (Fig. 2).

3.1.4. Calorimeter

The calorimeter was a powerful device for the identification of electromagnetic showers in a vast background of noninteracting particles and hadronic showers. Because of the limited thickness (7 radiation lengths), the calorimeter did not fully contain the electromagnetic showers induced by electrons with energy larger than a few hundred MeV. Yet, the longitudinal and transverse segmentation of the calorimeter combined with the measurement of the energy lost by the particle in each silicon strip resulted in a high

identification power for electromagnetic showers combined with a high rejection power for hadronic particles. The following information of the electromagnetic showers was found most useful for the identification (Boezio 1998):

1. the starting point of the shower;
2. the energy-momentum match;
3. the longitudinal profile;
4. the transverse profile;
5. the topological development of the shower.

Selection criteria based on the above features were used. These criteria were chosen with rigidity dependence (mainly a logarithmic dependence) and were based on (1) results from tests using particle beams at CERN (Bocciolini et al. 1993), (2) simulations (Boezio 1998), and (3) experience gained from a previous flight with the same instrument (Golden et al. 1996). Below 10 GeV, the same criteria were used for electrons and positron in order to make an accurate comparison of the fluxes. However, above 10 GeV, only electrons were selected and a looser calorimeter selection could be used, which thus led to higher statistics.

Figure 3 shows a quantity related to the topological development of the shower in the calorimeter as a function of particle rigidity. This quantity is the product of the sum of the number of hits inside a cylinder, of radius about 3 Molière units (8.5 calorimeter strips) with its axis along the particle direction, and the corresponding calorimeter plane number. The direction of the particle in the calorimeter was obtained from an extrapolation of the fitted track in the tracking system. This quantity strongly emphasizes the typical multiplication with increasing calorimeter depth of the secondaries of the electromagnetic cascades and their collimation along the track. For pure electromagnetic events, large values of this quantity were obtained. Clearly, for a hadronic shower, the transversal dispersion of the cascade and the limited number of secondaries usually

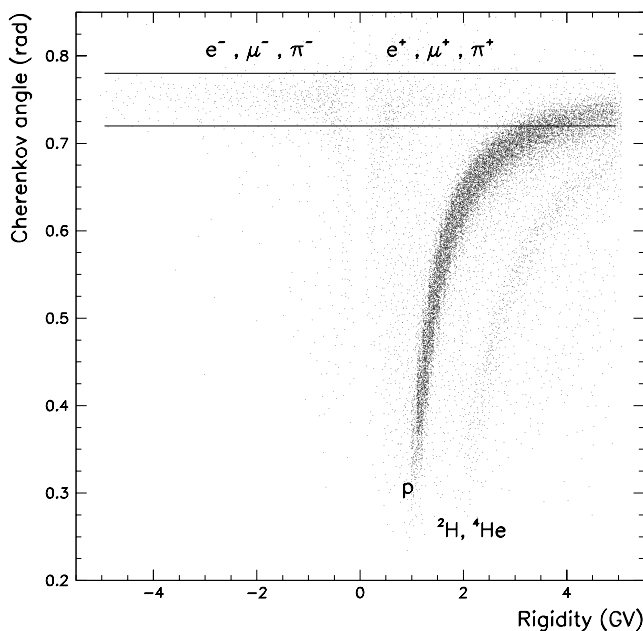


FIG. 2.—Measured RICH Cerenkov angle from flight data (about 410,000 events of which about 8000 are negative). In this and in the following figures, a negative sign has been assigned to the rigidity of negative particles. The solid lines comprise the events accepted as electrons in the RICH selection.

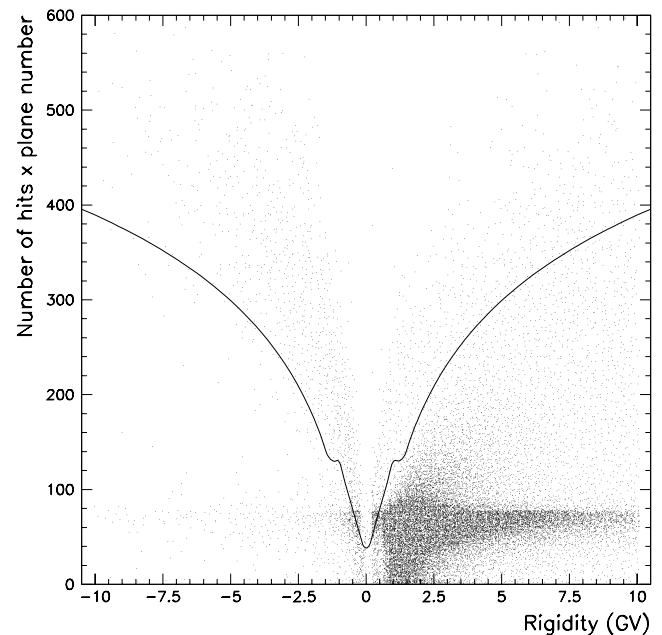


FIG. 3.—Topological development of the shower. The figure shows the sum of the number of hits inside $3R_M$ around the track multiplied by the corresponding calorimeter plane number vs. rigidity. The events above the solid line are tagged as electrons by this selection. The figure comprises about 516,000 events, of which about 15,000 are negative particles.

resulted in low values of this variable. On the negative side of Figure 3, the two components, namely, electrons and noninteracting particles (there can be also a small fraction of interacting pions) are clearly separated. On the positive side, both interacting and noninteracting protons appear mainly below the solid line. Only a small fraction of the proton events is in the region above the line where electrons appear on the negative side. Thus, positrons fall in the area above the solid line.

The transversal segmentation of the calorimeter permitted identification of electrons and positrons that emitted bremsstrahlung photons before entering the calorimeter (e.g., in the RICH or the aluminum cover of the gondola) by detecting the accompanying shower in the calorimeter. A 1.32 GeV positron inducing an electromagnetic shower accompanied by a second shower in the calorimeter is shown in Figure 4. The bending of the electron in the magnetic field is such that the electromagnetic shower induced by the photon is clearly separated in the two views. The radiation process at this energy is a unique feature of electrons. Hence, these double-shower events with a single track in the tracking system were clearly electron/positron events and could be identified with looser selection conditions.

It is worth pointing out that for electromagnetic showers the total energy measured in the calorimeter is related to the

energy of the incoming electrons. The experimental relation used in the analysis was in excellent agreement with the simulated one, which not only provides the reliability of the energy estimate of the electron independently by the calorimeter but also provides a confirmation of the rigidity measurement by the tracking system.

3.1.5. The Bar

A 17 kg, 1.2 m long aluminum bar with a 7 kg steel hook in the center was used to connect the payload to the balloon. This bar was situated 2.3 m above the RICH. The particle loss caused by interaction and production of secondary particles in the nonuniform I-shaped bar cannot be estimated reliably; hence, we chose to reject all particles crossing it. This was carried out by extrapolating the tracks to the position of the bar. This procedure resulted in a 10% reduction of the geometrical factor.

3.1.6. The Electron and Positron Samples

Figure 5 is similar to Figure 2 and shows the measured Cerenkov angle (RICH criteria 1–3) for (1) minimum ionizing particles and (2) after the further electron selection in the calorimeter. The powerful rejection of protons performed by the calorimeter selection can be noticed. The remaining proton contamination was easily removed by

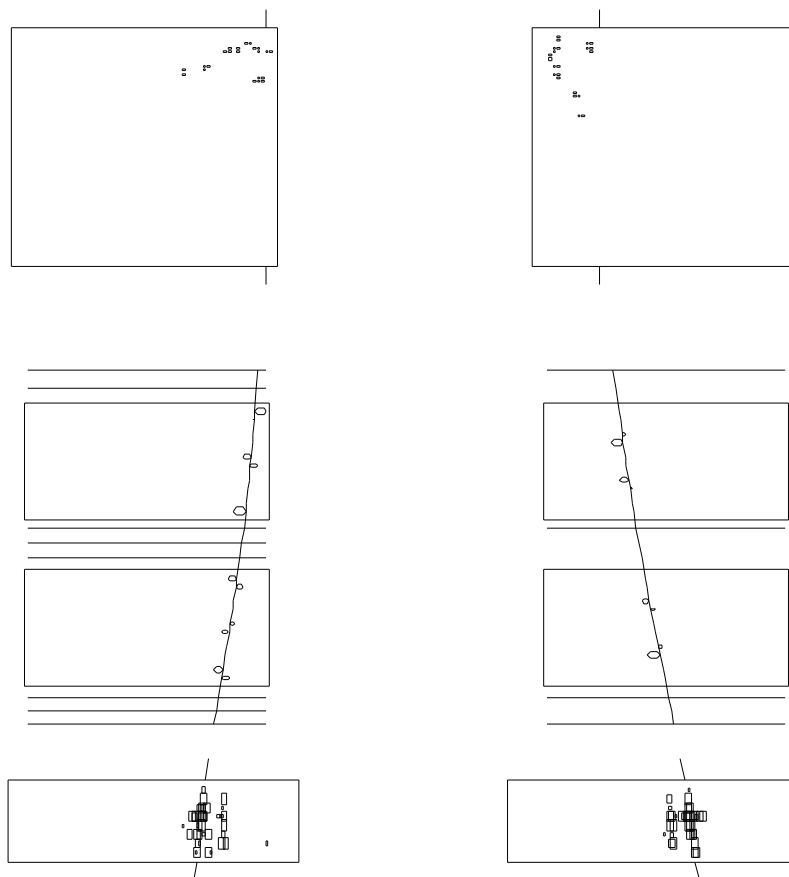


FIG. 4.—Display of a single 1.32 GeV positron in the CAPRICE94 instrument. The positron emits, according to the intersection of an extrapolation of the track, a bremsstrahlung photon in the RICH. From top to bottom are shown the RICH as seen from above, the tracking system, and the calorimeter. Note that the figure is not to scale, e.g., the calorimeter is significantly thinner than shown in the figure. For the track fit, only the drift chambers are used. The circles in the DCs indicate hits and their radius is proportional to the drift time. The bending view (x) is to the left and the nonbending view (y) to the right. The calorimeter shows the two electromagnetic showers produced by the positron and by the bremsstrahlung photon, respectively.

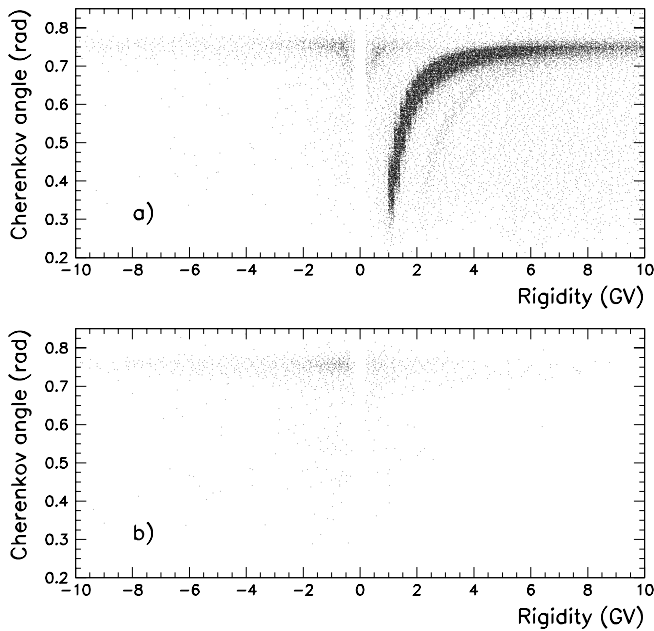


FIG. 5.—Measured RICH Cerenkov angle from flight data for (a) particles after ToF and dE/dx electron selection (354,994 events) and (b) calorimeter electron selection (4267 events).

applying the last RICH criterion. Before the application of the RICH selection based on the Cerenkov angle (RICH criterion 4), there were (Fig. 5b) 3428 negative and 839 positive events in the rigidity bin from 0.3 to 10 GV. After applying the RICH criterion on the Cerenkov angle, 3174 electrons and 734 positron remained. The second and third

columns of Table 1 show the number of events, both negative and positive, surviving each detector selection.

3.2. Contamination

3.2.1. Proton Contamination

The number of protons passing the RICH cuts was estimated using a proton sample selected by the ToF below 1 GV from the particle velocity and by the calorimeter above 1 GV by requiring a hadronic interaction in the calorimeter volume. The RICH selection criteria were applied to this proton sample and the surviving protons were used to determine the contamination. The proton contamination in the RICH was found to be less than 0.1% up to 1.2 GV, at which point the protons were below the RICH threshold. Above the RICH threshold, the contamination slowly increased to 2% at 3 GV and then to 30% at 4 GV and 60% at 5 GV. Above this rigidity, protons became indistinguishable from $\beta \approx 1$ particles.

To estimate the number of protons that simulated a positron-like cascade in the calorimeter, we selected a proton sample using the RICH and the ToF for rigidities less than 1.2 GV. In this energy region, the RICH acted as a threshold counter and the ToF was able to separate protons from lighter particles. Between 1.2 and 5 GV, the RICH could identify protons. The proton contamination in the calorimeter selection was found to be $\approx 7 \times 10^{-4}$ for rigidities below 1 GV; $\approx 7 \times 10^{-5}$ between 1 and 3 GV and $\approx 1.5 \times 10^{-4}$ above 3 GV. It was not possible to select a clean proton sample above 5 GV, so the calorimeter proton rejection factor was assumed to be the same as that in the 3–5 GV bin. This can be justified by the fact that the proton inelastic cross section is rather constant over the momentum interval 3–10 GeV c^{-1} and similar hadronic shower

TABLE 1
SUMMARY OF ELECTRON AND POSITRON RESULTS

ENERGY BIN AT THE SPECTROMETER (GeV)	SELECTED EVENTS ^a		FLUX IN THE SPECTROMETER ^b (GeV m ² sr s) ⁻¹	
	e^-	e^+	e^-	e^+
0.3–0.4	147	100	$(3.1 \pm 0.3) \times 10^1$	$(2.2 \pm 0.3) \times 10^1$
0.4–0.5	204	84	$(2.8 \pm 0.2) \times 10^1$	$(1.2 \pm 0.1) \times 10^1$
0.5–0.6	207	71	$(2.3 \pm 0.2) \times 10^1$	8 ± 1
0.6–0.7	210	70	$(2.0 \pm 0.2) \times 10^1$	7.0 ± 0.9
0.7–0.8	202	55	$(1.8 \pm 0.1) \times 10^1$	5.1 ± 0.7
0.8–0.9	152	48	$(1.3 \pm 0.1) \times 10^1$	4.2 ± 0.6
0.9–1	160	29	$(1.4 \pm 0.1) \times 10^1$	2.5 ± 0.5
1–1.25	331	77	$(1.1 \pm 0.1) \times 10^1$	2.6 ± 0.3
1.25–1.5	278	39	9.1 ± 0.6	1.3 ± 0.2
1.5–1.75	232	38	7.6 ± 0.6	1.3 ± 0.2
1.75–2	195	21	6.4 ± 0.5	$(6.9^{+1.9}_{-1.5}) \times 10^{-1}$
2–2.25	149	12	4.9 ± 0.4	$(4.0^{+1.5}_{-1.1}) \times 10^{-1}$
2.25–2.5	92	11	3.1 ± 0.3	$(3.7^{+1.5}_{-1.1}) \times 10^{-1}$
2.5–3	177	21	3.0 ± 0.3	$(3.5^{+1.0}_{-0.8}) \times 10^{-1}$
3–3.5	107	13 (0.5)	1.8 ± 0.2	$(2.1^{+0.8}_{-0.6}) \times 10^{-1}$
3.5–4	79	7 (1.2)	1.3 ± 0.2	$(9.8^{+6.6}_{-4.5}) \times 10^{-2}$
4–5	93	9 (2.5)	$(7.9 \pm 0.9) \times 10^{-1}$	$(5.5^{+3.8}_{-2.7}) \times 10^{-2}$
5–7	106	22 (5)	$(3.3 \pm 0.4) \times 10^{-1}$	$(5.4^{+2.1}_{-1.6}) \times 10^{-2}$
7–10	53	7 (3.2)	$(1.2 \pm 0.2) \times 10^{-1}$	$(8.2^{+9.5}_{-6.4}) \times 10^{-3}$
10–14	20	...	$(3.4^{+1.9}_{-0.8}) \times 10^{-2}$...
14–19	12	...	$(1.7^{+0.9}_{-0.5}) \times 10^{-2}$...
19–30	5	...	$(3.2^{+2.1}_{-1.4}) \times 10^{-3}$...

^a The numbers shown in the brackets are the estimated proton background.

^b The quoted errors are a combination of statistical and systematic errors.

topology can be expected in the calorimeter. Furthermore, the proton contamination of the calorimeter selection between 5 and 10 GV has been verified (Boezio et al. 1999c) by measurements with a later balloon-borne experiment, CAPRICE98, where the same calorimeter was used along with a gas-RICH detector that could identify protons in this rigidity range.

The independent proton contaminations thus determined gave a proton rejection factor of more than 10^6 up to 3 GV for the combined RICH and calorimeter selection for positrons. Furthermore, below 1 GV the dE/dx selection significantly reduced the proton background. All these permitted the identification of electrons and positrons with a negligible contamination (less than 1% of the positron sample) up to 3 GV. Above 3 GV, the proton contamination was estimated to be 14% of the positron sample in the rigidity bin 3–5 GV. In the rigidity region 5–10 GV, only the calorimeter was used, which resulted in a proton contamination of 28% of the selected positron sample. This proton contamination is shown in parentheses in Table 1 and was subtracted from the positron sample.

3.2.2. Muon and Pion Contamination

Muons were efficiently separated from electromagnetic showers in the calorimeter by their noninteracting character, and their contamination could safely be assumed to be negligible (Boezio 1998).

The pion contamination in the calorimeter selection was studied using simulations. Using the electron selection criteria on the pion sample, about 1% of the simulated pions for momenta below 1 GeV c^{-1} passed and of the order of 0.1% for higher momenta. However, the abundance of pions in the selected minimum ionizing sample is a small fraction of the muon component (Boezio 1998; Boezio et al. 1999b). Hence, the pion contamination amounted to less than 1% of the electron and positron samples.

Except for rigidities below 500 MV, the RICH could not separate muons and pions from electrons and positrons.

3.2.3. Heavier Nuclei Contamination

The combined dE/dx , RICH, and calorimeter selections reduced the contamination of heavier nuclei, which is made up of mainly helium nuclei, to a negligible fraction of the positron sample.

3.3. Efficiency

As shown above, the CAPRICE94 detectors identified electrons and positron with very small backgrounds. We also needed to accurately determine the efficiency of each detector, resulting from the particle selection criteria invoked in the analysis, in order to determine the fluxes of the different particle types reliably. To determine the efficiency of a given detector, a data set of electrons, selected by the remaining detectors, was constructed. The number of electrons identified as electrons by the detector being tested, divided by the number of events in the data set, provided a measure of the efficiency. This procedure was repeated for each detector. In this delicate process, systematic errors could come from incorrect assumptions of correlations between selections or from biased samples, but we believe that the systematic errors are very small in our analysis. The resulting efficiencies for electrons as a function of rigidity are shown in Figure 6 and are discussed in detail below along with possible systematic uncertainties.

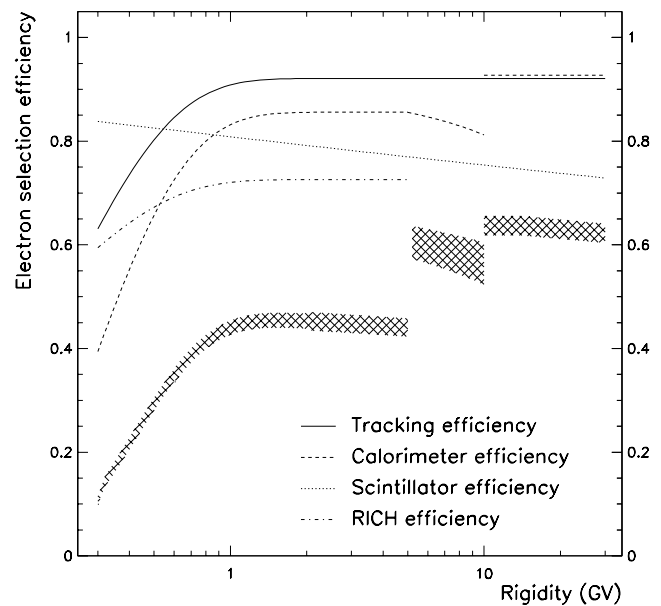


FIG. 6.—Electron selection efficiencies as a function of rigidity. The cross-hatched area indicates the 1σ confidence interval of the combined efficiency.

The efficiency of each detector was determined as a function of rigidity in a number of discrete bins. We then parameterized the efficiency to allow an interpolation between bins. This parameterization introduced a systematic error on the efficiency of each detector. Since the parameters were correlated, the error on the efficiency was obtained using the error matrix of the fit for each detector when correcting the measured flux for the detector efficiencies.

3.3.1. Tracking Efficiency

The tracking efficiency was obtained from test samples of negative singly charged particles selected by the other detectors. Since the amount of material in the tracking system was very small, the probability of pair conversion of the bremsstrahlung photons, which were produced anywhere above the tracking system, was negligible inside the tracking system. Conversion of photons in the material above the tracking system was eliminated by the RICH and dE/dx selection on the top scintillators. Hence, the tracking efficiency for electrons and muons could be assumed to be the same.

A sample of singly charged particles was selected requiring a single ionization cluster in the RICH and a dE/dx signal in the top scintillator typical of a minimum ionizing particle. From this sample, negatively charged events were selected by requiring a negative deflection from the fit to the MWPC trajectory measurements. The contamination of spillover protons was eliminated by requiring that the measured impact positions in the RICH and calorimeter nearly match the positions as obtained by extrapolating the particle trajectory derived from the MWPC fit. The resulting sample of negative singly charged particles was used to determine the efficiency of fitting tracks in the drift chamber system.

The assumption of identical tracking efficiency for muons and electrons was tested by restricting the efficiency to a sample of events having a large number of hits in the calorimeter. The resulting efficiency was in agreement with the

efficiency estimated using the whole negative sample. The latter one was used because of the higher statistics.

Biases in the efficiency sample were studied using protons (see Weber 1997). It was found that the criteria used for fitting the tracks using the MWPC reduced slightly the number of scattered tracks in the sample. To account for this reduction, a systematic uncertainty of 2% was introduced (Boezio 1998).

Possible charge sign dependence of the efficiency was studied using both the flight data and the data taken on the ground before the flight. No significant dependence was found above 0.3 GV (Boezio 1998).

Since the estimation of the efficiency of the drift chamber system relied on the track determination by the MWPC system, a cross-check of the measured efficiency was performed on an event-by-event basis. A large sample of events with a single track in the RICH and in the top scintillator with a well-developed electromagnetic shower in the calorimeter was selected. This sample consisted mostly of high-energy electrons, along with some interacting protons and a few multiple track events. All these events were visually scanned and the electrons were identified. On these events, the criteria for track selection were applied. The resultant efficiency was slightly ($\approx 7\%$) lower than that of the one estimated using the MWPC system. Since the procedure was not free of ambiguities (the electron sample could still be contaminated by protons), it was used as a measure of an additional systematic uncertainty. This uncertainty was not added to the flux data but should be considered as part of an overall systematic uncertainty of the flux measurements presented in this paper (see the discussion of systematic uncertainties in § 3.5).

3.3.2. Scintillator Efficiency

The dE/dx selection efficiency was estimated using simulated electrons, and the results were compared with an experimental efficiency obtained using a sample of electrons identified by the calorimeter.

First, the simulation of the payload was tuned to reproduce the energy losses in the ToF scintillator for muons from ground and flight data. Then several tens of thousands of electrons were simulated according to an input spectrum that reproduced the experimental spectrum in the spectrometer. The energy dependence of the efficiency could be related to the probability that an electron radiated a photon that converted in or above the top scintillator. Hence, a simple relation between the energy measured in the spectrometer and the simulated scintillator efficiency was found. Finally, the simulated efficiency was compared with an experimental estimation in the rigidity range 1–10 GV and a good agreement was found (see Boezio 1998 for more details). The scintillator efficiency is shown as a dotted line in Figure 6. The near logarithmic dependence of this efficiency with energy is related to the total number of photons radiated by the electron above a given energy. A systematic uncertainty of 1% is quadratically summed to the efficiency uncertainties to account for simulation uncertainties.

3.3.3. RICH Efficiency

The efficiency of the RICH electron selection was determined experimentally. An electron sample was selected using the time of flight, the scintillator dE/dx , and the calorimeter. Both the calorimeter and the scintillator selection efficiencies were obtained without using the RICH; hence,

any possible bias introduced in these samples did not affect the result on the RICH selection efficiency. In fact, the RICH selection criteria were always applied to a sample of events that survived all the other selections.

The dash-dotted line in Figure 6 shows the efficiency for the RICH selection. Note that above 5 GV the RICH was not used in the analysis.

3.3.4. Calorimeter Efficiency

Since it was not possible to select an unbiased sample of electrons from flight data without using the calorimeter, the calorimeter selection efficiency was obtained from simulations. This was justified by the good agreement found between simulation results and the results from beam tests of the calorimeter (Boccolini et al. 1993). Furthermore, many experimental features of the electromagnetic shower in the calorimeter from the flight data were well reproduced by the simulations (Boezio 1998). As a cross-check, the simulated efficiency was compared with an experimental estimation between 0.5 and 20 GV, which used the calorimeter itself as a selector of the efficiency sample (see Boezio 1998 for more details). Throughout, a good agreement between the two efficiencies was found. Between 2 and 5 GV, the experimental data indicated a constancy of the efficiency of about 84% while the simulated efficiency increased slightly from $\approx 85\%$ at 2 GV to $\approx 89\%$ at 5 GV; then it decreased in agreement with the experimental estimation. To account for this difference, between 2 and 5 GV an intermediate efficiency of $\approx 86\%$ was used with an additional systematic error of 2%. Above 10 GV, a looser selection was used for the electron analysis, which gave an increased selection efficiency of about 93%. The dashed line in Figure 6 shows the calorimeter efficiency.

3.4. Electron and Positron Spectra at the Top of the Atmosphere

To obtain the electron and positron fluxes at the top of the atmosphere, several corrections must be made. The number of e^- and e^+ candidates must be corrected for the selection efficiencies and the e^- and e^+ spectra in the spectrometer have to be obtained by considering both the geometrical factor and live time of the experiment. These spectra must be propagated backward to the top of the payload by taking into account, e.g., bremsstrahlung losses, and then secondary e^- and e^+ spectra produced in the overlying atmosphere have to be subtracted from the experimental spectra. Finally, the e^- and e^+ spectra must be propagated back to the top of the atmosphere.

3.4.1. Electron and Positron Fluxes in the Spectrometer

Since the efficiencies were rigidity dependent, the rigidity range under study was split into sections of 50 MV wide bins. Given the small bin width, the efficiencies were assumed not to vary (relative variation less than 10%) within the bins. This was possible up to 2 GV, and above this rigidity the statistics became too small to allow this fine binning; therefore, larger bins were used. However, above 2 GV all the efficiencies and the geometrical factor were nearly constant.

The values of the e^- and e^+ fluxes ($J_{\text{spe}}^{e^-,e^+}$) in the spectrometer were obtained according to

$$J_{\text{spe}}^{e^-,e^+}(E) = \frac{1}{T_{\text{live}} \times G^{e^-,e^+} \times \epsilon \times \Delta E} \times N_{\text{spe}}^{e^-,e^+}(E), \quad (1)$$

where T_{live} is the live time, G^{e^-,e^+} are the geometrical factors for electrons and positrons, ϵ is the combined selection efficiency, ΔE is the width of the energy bin, E the kinetic energy, and $N_{\text{spe}}^{e^-,e^+}(E)$ is the selected number of e^- and e^+ in the spectrometer as given in Table 1. The analysis was based on 60,520 s of data taken over a total acquisition time of 18 hr. The fractional live time during the flight was 0.2690 ± 0.0006 , resulting in a total live time of 16280 ± 36 s. The geometrical factor was obtained with simulation techniques (Sullivan 1971). The geometrical factor varied with rigidity decreasing (the decrease is mainly caused by the geometrical condition on the bar) from ≈ 174 at 0.3 GV to $\approx 166 \text{ cm}^2 \text{ sr}$ at 1 GV for e^- and from ≈ 168 at 0.3 GV to $\approx 164 \text{ cm}^2 \text{ sr}$ at 1 GV for e^+ . Above 1 GeV, the geometrical factor was the same for e^- and e^+ and constant at about $163 \text{ cm}^2 \text{ sr}$. The resulting electron and positron fluxes in the spectrometer are given in Table 1. The mean energies of the bins are given according to Lafferty & Wyatt 1995.

3.4.2. Electron and Positron Fluxes at the Top of the Payload

Electrons and positrons crossing the material above the tracking system lost energy by ionization and bremsstrahlung processes. This changed the energy distribution of these particles and, hence, the electron and positron spectra determined in the spectrometer were extrapolated to the top of the payload by solving the cascade equation using an iterative Runge-Kutta technique. The results were cross-checked using the simulation of the payload. These fluxes are given in Table 2 and are shown in Figure 7.

3.4.3. Atmospheric Secondary Electrons and Positrons

The dashed and solid curves shown in Figure 7 are, respectively, the e^+ and e^- spectra of secondary electrons

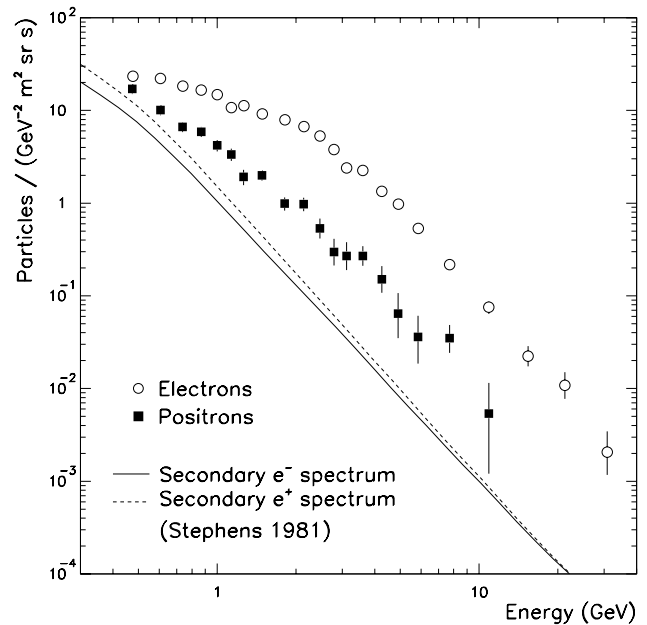


FIG. 7.—Experimental electron and positron spectra at top of the payload and the calculated atmospheric electrons (solid line) and positrons (dashed line) at 3.9 g cm^{-2} of residual atmosphere (Stephens 1981).

produced by the interactions of cosmic-ray nuclei in the overlying atmosphere (Stephens 1981). These calculated atmospheric electron and positron fluxes are also tabulated in Table 2.

Reentrant albedo particles, i.e., albedo particles produced in the opposite hemisphere which escape the atmosphere with rigidity less than the local geomagnetic threshold rigidity and are bent back into the atmosphere by the Earth

TABLE 2
ELECTRON AND POSITRON FLUX AT THE TOP OF THE PAYLOAD

MEAN ENERGY AT TOP OF THE PAYLOAD (GeV)	FLUX AT TOP OF THE PAYLOAD ^a (GeV m ² sr s) ⁻¹		ATMOSPHERIC SECONDARY FLUX (GeV m ² sr s) ⁻¹	
	e^-	e^+	e^-	e^+
0.48.....	$(2.3 \pm 0.2) \times 10^1$	$(1.7 \pm 0.2) \times 10^1$	0.81×10^1	1.23×10^1
0.61.....	$(2.2 \pm 0.2) \times 10^1$	$(1.0 \pm 0.1) \times 10^1$	0.44×10^1	0.66×10^1
0.74.....	$(1.8 \pm 0.1) \times 10^1$	6.7 ± 0.8	0.26×10^1	3.79
0.87.....	$(1.7 \pm 0.1) \times 10^1$	5.9 ± 0.7	0.16×10^1	2.32
1.00.....	$(1.5 \pm 0.1) \times 10^1$	4.2 ± 0.6	0.10×10^1	1.50
1.13.....	$(1.1 \pm 0.1) \times 10^1$	3.4 ± 0.5	0.07×10^1	1.03
1.26.....	$(1.1 \pm 0.1) \times 10^1$	1.9 ± 0.4	0.05×10^1	0.74
1.49.....	9.2 ± 0.6	2.0 ± 0.2	0.31	0.44
1.81.....	7.9 ± 0.5	$(9.9 \pm 1.6) \times 10^{-1}$	0.17	2.38×10^{-1}
2.14.....	6.7 ± 0.5	$(9.8 \pm 1.6) \times 10^{-1}$	0.11	1.41×10^{-1}
2.47.....	5.3 ± 0.4	$(5.3^{+1.5}_{-1.2}) \times 10^{-1}$	0.07	0.90×10^{-1}
2.79.....	3.8 ± 0.3	$(3.0^{+1.1}_{-0.9}) \times 10^{-1}$	0.05	0.61×10^{-1}
3.12.....	2.4 ± 0.3	$(2.7^{+1.1}_{-0.8}) \times 10^{-1}$	0.03	0.43×10^{-1}
3.60.....	2.3 ± 0.2	$(2.7^{+0.7}_{-0.6}) \times 10^{-1}$	0.02	0.27×10^{-1}
4.26.....	1.3 ± 0.1	$(1.5^{+0.6}_{-0.4}) \times 10^{-1}$	0.01	0.16×10^{-1}
4.91.....	$(9.8 \pm 1.2) \times 10^{-1}$	$(6.4^{+4.3}_{-2.9}) \times 10^{-2}$	0.08×10^{-1}	1.04×10^{-2}
5.86.....	$(5.3 \pm 0.6) \times 10^{-1}$	$(3.6^{+2.5}_{-1.8}) \times 10^{-2}$	0.05×10^{-1}	0.59×10^{-2}
7.71.....	$(2.2 \pm 0.2) \times 10^{-1}$	$(3.5^{+1.4}_{-1.1}) \times 10^{-2}$	0.02×10^{-1}	0.25×10^{-2}
10.89.....	$(7.5 \pm 1.1) \times 10^{-2}$	$(5.4^{+6.2}_{-4.1}) \times 10^{-3}$	0.08×10^{-2}	0.87×10^{-3}
15.4.....	$(2.2^{+0.6}_{-0.5}) \times 10^{-2}$...	0.03×10^{-2}	...
21.2.....	$(1.1^{+0.4}_{-0.3}) \times 10^{-2}$...	0.01×10^{-2}	...
30.9.....	$(2.1^{+1.4}_{-0.9}) \times 10^{-3}$...	0.04×10^{-3}	...

^a The quoted errors are a combination of statistical and systematic errors.

magnetic field, were not considered since the measurements presented in this paper are above the geomagnetic cutoff.

The correctness of the calculated secondary spectra used in this work was checked by studying the muon fluxes. At the atmospheric depth of 3.9 g cm^{-2} , secondary electrons and positrons come mainly from muon decay. Figure 8 shows the positive (*solid squares*) and negative (*open circles*) spectra of muons measured by this experiment (Boezio 1998; Boezio et al. 1999b) along with the calculated spectra (μ^+ : *dashed line*; μ^- : *solid line*). The calculated fluxes are given by the same calculation (Stephens 1981) used for the secondary electrons and positrons. The μ^+ flux values are shown only up to 2 GeV because above this energy the experiment cannot efficiently reject the proton contamination. A good agreement between the measured and calculated spectra was found.

A further check was performed measuring the electron and positron fluxes as a function of atmospheric depth from 3.9 to 990 g cm^{-2} in the energy range 0.8–1.2 GeV (mean energy of 980 MeV). These fluxes were compared with the atmospheric growth curves calculated by Daniel & Stephens 1974 for electrons and positrons of energy 1 GeV for a location with zero geomagnetic cutoff and during minimum solar activity. A rather good agreement (experimental data lower than the calculation of the order of 25%) was found between the data and the theoretical curves (Boezio 1998). The atmospheric secondary calculation used in this work (Stephens 1981) is an updated version of the work of Daniel & Stephens (1974) giving slightly lower secondary fluxes. It made use of newer accelerator data and it was performed only for small atmospheric depths.

3.4.4. Electron and Positron Fluxes at the Top of the Atmosphere

The electron and positron spectra at the top of the payload were corrected for the atmospheric secondaries and were then propagated back to the top of the atmosphere by simultaneously solving the cascade equations describing the propagation of electrons, positrons, and secondary gamma

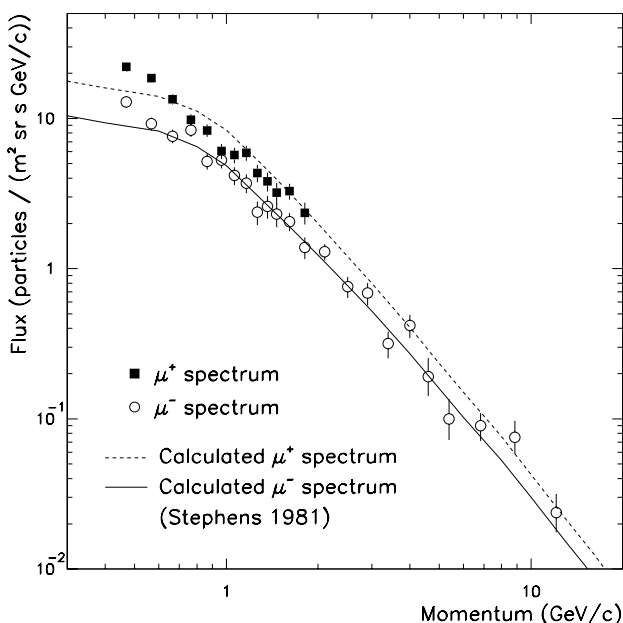


FIG. 8.—Experimental positive and negative muon spectra along with the calculated μ^+ (*dashed line*) and μ^- (*solid line*) spectra at 3.9 g cm^{-2} of residual atmosphere (Stephens 1981).

rays. The resulting fluxes at the top of the atmosphere are presented in Table 3.

3.5. Systematic Uncertainties

Systematic uncertainties originating from the determination of the detector efficiencies were included in the data points as discussed in § 3.3. Another possible systematic error was related to the efficiency of the trigger system. The performance of each photomultiplier pair was tested comparing the spatial distribution of triggers in this experiment with that given by the simulation used for the geometrical factor. The excellent agreement between the simulated and experimental distributions permitted the conclusion that a possible systematic error caused by a geometrical inefficiency of the trigger was less than 1%.

The iterative back propagation of the spectra to the top of the payload and to the top of the atmosphere required a smoothing of the experimental data points. The spectral shapes resulting from such smoothing are known only with the precision of the experimental data and, hence, this procedure contributes to the experimental uncertainty of the propagated fluxes. A systematic uncertainty of 5%, which was obtained using different acceptable smoothing algorithms of the spectra, was introduced to account for this procedure. Another method was also used in the literature (e.g., Barwick et al. 1998), which was introduced by Schmidt (1972). In this method, he integrated the cascade equation given by Rossi and obtained a simple relation between the electron spectrum at different depths, assuming that the spectrum follows a power law in energy. Even if this method appeals for its simplicity, it has two problems: it works only for spectra that follow a power law and the spectral index of the power law must be known. This spectral index is obtained from the data and, consequently, it has an error caused by the experimental uncertainty. This error affects the resulting flux at the top of the atmosphere similarly to what happens with the procedure used in this work.

The residual atmosphere above the gondola was measured by two pressure sensors owned and calibrated by the National Scientific Balloon Facility. Conservatively speaking, a systematic error of 10% was assumed, resulting in a mean residual atmospheric depth of $3.9 \pm 0.4 \text{ g cm}^{-2}$. This affected both the propagation of the spectra and the calculation of the secondaries. The effect on the propagation was a shift of $\approx \pm 1\%$ on the mean energy for both electrons and positrons. Instead, the effect on the secondary subtraction, caused by the uncertainty in the atmospheric depth, is more important for positrons than for electrons. The uncertainty of the positron flux could be as large as 25% at 0.5 GeV, decreasing to $\approx 1\%$ at 10 GeV. For electrons, it was of the order of 5% at 0.5 GeV, decreasing to less than 1% above 1 GeV.

Similar systematic errors are caused by the uncertainty on the secondary production in the atmosphere. As shown in § 3.4.3, the calculation that gave secondary electron and positron fluxes also gave muon spectra in good agreement with the experimental ones. Hence, a 10% uncertainty can be reasonably assumed on these calculations.

The geometrical factor was cross-checked with two other methods. One adopted the same approach as presented in Sullivan (1971), using, however, a different method to trace the particles: the track fitting algorithm used in the analysis was also used to trace the particle through the spectrometer. This method gave the same results within 1% at all rigi-

TABLE 3
ELECTRON AND POSITRON FLUX AT THE TOP OF THE ATMOSPHERE

ENERGY BIN AT TOA (GeV)	MEAN ENERGY AT TOA (GeV)	FLUX ^a AT TOA ^b (GeV m ² sr s) ⁻¹	
		Electrons	Positrons
0.46–0.61	0.54	$(1.3 \pm 0.2) \times 10^1$	3.9 ± 1.7
0.61–0.75	0.68	$(1.6 \pm 0.2) \times 10^1$	3.2 ± 1.1
0.75–0.90	0.83	$(1.5 \pm 0.1) \times 10^1$	2.7 ± 0.8
0.90–1.05	0.97	$(1.4 \pm 0.1) \times 10^1$	3.4 ± 0.7
1.05–1.19	1.12	$(1.3 \pm 0.1) \times 10^1$	2.5 ± 0.5
1.19–1.34	1.26	9.3 ± 0.9	2.1 ± 0.5
1.34–1.48	1.41	10.0 ± 0.9	1.1 ± 0.3
1.48–1.84	1.66	8.4 ± 0.6	1.4 ± 0.2
1.84–2.21	2.02	7.4 ± 0.5	$(6.8 \pm 1.5) \times 10^{-1}$
2.21–2.57	2.39	6.3 ± 0.5	$(7.6 \pm 1.5) \times 10^{-1}$
2.57–2.93	2.75	4.9 ± 0.4	$(3.9^{+1.3}_{-1.0}) \times 10^{-1}$
2.93–3.30	3.11	3.3 ± 0.3	$(2.1^{+1.0}_{-0.7}) \times 10^{-1}$
3.30–3.66	3.48	2.1 ± 0.2	$(2.0^{+0.9}_{-0.7}) \times 10^{-1}$
3.66–4.39	4.01	2.0 ± 0.2	$(2.1^{+0.6}_{-0.5}) \times 10^{-1}$
4.39–5.11	4.74	1.2 ± 0.1	$(1.2^{+0.3}_{-0.4}) \times 10^{-1}$
5.11–5.84	5.47	$(8.4 \pm 1.0) \times 10^{-1}$	$(4.6^{+3.7}_{-2.5}) \times 10^{-2}$
5.84–7.29	6.51	$(4.5 \pm 0.5) \times 10^{-1}$	$(2.5^{+2.1}_{-1.5}) \times 10^{-2}$
7.29–10.20	8.58	$(1.8 \pm 0.2) \times 10^{-1}$	$(2.7^{+1.1}_{-0.9}) \times 10^{-2}$
10.20–14.56	12.11	$(6.3 \pm 1.0) \times 10^{-2}$	$(3.7^{+5.1}_{-3.5}) \times 10^{-3}$
14.6–20.4	17.1	$(1.9^{+0.5}_{-0.4}) \times 10^{-2}$...
20.4–27.6	23.6	$(9.1^{+3.5}_{-2.6}) \times 10^{-3}$...
27.6–43.6	34.3	$(1.7^{+1.2}_{-0.8}) \times 10^{-3}$...

^a The quoted errors are a combination of statistical and systematic errors.

^b Top of the Atmosphere.

dities. The second used a numerical integration calculation of the geometrical factor that agreed with the previous results within 2% above 0.5 GV and within 5% below 0.5 GV. From this, the systematic error caused by the geometrical factor calculation was less than 5% between 0.3 and 0.5 GV and less than 2% for rigidities higher than 0.5 GV.

The extrapolation of the calorimeter proton rejection factor from the bin 3–5 GV to the bins 5–7 GV and 7–10 GV introduced an uncertainty on the estimation of the proton background and, consequently, on the positron fluxes. Assuming an uncertainty on the rejection factor of 50%, a systematic error of $\approx 20\%$ at 8.6 GeV and of $\approx 50\%$ at 12.1 GeV is obtained on the positron flux at the top of the atmosphere.

Another source of uncertainty on the measured spectra was caused by the intrinsic spectrometer resolution. To obtain this systematic error, we used the same method presented in Boezio et al. 1999a. We assumed that the differential electron flux above 5 GV, where the finite spectrometer resolution has a measurable effect, is a power law in rigidity (R) of the type $A(R^{-\gamma})$ (with $\gamma = 3.2$), which we converted into a deflection spectrum. This deflection spectrum was then smeared by a Gaussian error distribution with a standard deviation parameter distribution deduced from the experimental data, peaked at $1/150 \text{ GV}^{-1}$. The smeared deflection distribution was then retransformed into a rigidity spectrum, and the ratio between the smeared spectrum and the input spectrum was used as a measure of the uncertainty caused by the finite spectrometer resolution. The error is only weakly dependent on the spectral index. The error systematic caused by the spectrometer resolution is small, increasing from less than 1% at 10 GV to about 2% at 30 GV.

We have added the different systematic uncertainties, which are uncorrelated, quadratically to obtain an overall systematic uncertainty, which is rigidity dependent, for positrons decreasing from $\approx 35\%$ at 0.5 GeV to $\approx 10\%$ above 1 GeV, then becoming $\approx 22\%$ at 9 GeV and $\approx 50\%$ at 12 GeV. For electrons, the estimated systematic errors decrease from $\approx 15\%$ at 0.5 GeV to less than 10% above 1 GeV. Furthermore, as discussed in § 3.3.1, an additional systematic uncertainty of 7% has to be included to account for the uncertainty of the tracking efficiency. Since the tracking efficiency could be overestimated by this quantity, the electron and positron fluxes could be underestimated by approximately 8% (the tracking efficiency is $\approx 92\%$ above 0.8 GeV). These uncertainties were not included in the data presented in the tables and the figures.

4. RESULTS

4.1. Experimental Results at Top of the Atmosphere

Figure 9 shows the CAPRICE94 electron flux (multiplied by E^3 , where E is the energy in GeV) at the top of the atmosphere as a function of energy, together with other experimental results obtained in the last three decades, and some theoretical predictions (see § 4.2). This figure includes only those results obtained from experiments that could distinguish e^- from e^+ . Among these, there are results from three experiments carried out by the WIZARD collaboration, namely, MASS89 (Golden et al. 1994), MASS91 (Basini et al. 1995),⁴ and CAPRICE94 (this work), which used the same superconducting magnet and similar tracking devices. Of these experiments, the tracking systems were

⁴ Results partially modified subsequently: F. Cafagna, 1999, private communication.

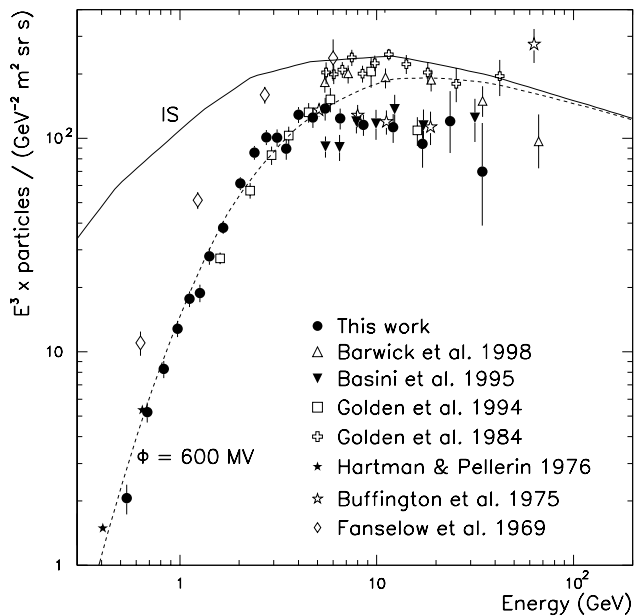


FIG. 9.—Electron spectrum multiplied by E^3 (E is the energy in GeV) measured by CAPRICE94 and other balloon-borne experiments. The solid line labeled IS is the calculated interstellar electron spectrum using a diffusive-halo model with momentum-dependent Galactic propagation of the cosmic rays (Moskalenko & Strong 1998). The dashed line is the same spectrum modulated according to eq. (2) with a modulation parameter $\phi = 600$ MV.

improved in MASS91 and in CAPRICE94 with respect to MASS89 by the introduction of two drift chambers. Furthermore, the calorimeter, the main electron identifying detector, was improved significantly in the CAPRICE94 experiment by replacing the brass-streamer tube calorimeter used in the other two experiments with a silicon-tungsten calorimeter. Above 10 GeV, where the effect of solar modulation is small, the results from these three experiments are in good agreement with each other. Only the MASS89 data point at 9 GeV differ significantly. At lower energies, the comparison between CAPRICE94 and MASS89, both launched from nearby locations in North Canada (MASS91 was launched from Fort Sumner, New Mexico, USA, with a geomagnetic cutoff higher than 4 GV), is difficult because these two balloon flights took place at two different periods of solar modulation. However, as expected, the MASS89 fluxes are lower since the experiment was performed during a period of higher solar activity (1989 September).

The High-Energy Antimatter Telescope (HEAT) collaboration has recently published results from a 1994 experiment (Barwick et al. 1998) launched from Fort Sumner, New Mexico. Their data on the electron flux in the energy range 5–100 GeV (the HEAT highest energy point is the sum of the electron and positron fluxes) is about 70% higher than the results we obtained during the same year but at a different location with lower geomagnetic cutoff. Because of the steep energy spectrum of electrons, a 20% systematic uncertainty in the energy estimation (the HEAT collaboration quotes an uncertainty of about 10% in Barwick et al. 1998) between the two experiments can explain this difference in the absolute fluxes. One can also notice from this figure that some of the earlier experiments (Fanselow et al. 1969; Golden et al. 1984) obtained flux values that are higher by about a factor of 2 compared with CAPRICE94

results. However, we emphasize once again the good agreement among the results from the three WIZARD experiments.

Figure 10 shows the CAPRICE94 positron flux (multiplied by E^3) at the top of the atmosphere, as a function of energy, together with other experimental results and theoretical estimates. It is clear from this figure that most of the experimental results are at energies above 4.5 GeV and that there is considerable scatter in the absolute flux values. It can be also seen that the errors associated with individual data points are very large, owing to low statistics; the better ones are those from the present experiment and the HEAT results. Considering the large errors associated with the flux values, there is general consistency among various measurements, as the observed scatter of data points in this figure is within 2σ .

In Table 4, the fraction of positrons obtained in this work is presented. To reduce the statistical error in determining the ratio, we combined the adjacent energy bins. These ratios are also shown in Figure 11 along with other experimental data and theoretical predictions. An excellent agreement is found among the CAPRICE94 results, the recent data from the WIZARD experiments, namely, MASS89 (Golden et al. 1994) and TS93 (Golden et al. 1996) and the combined HEAT results (Barwick et al. 1997). The earlier trend of a strong increase of the ratio for energies above 8 GeV is not present in the more recent data. Note that the published HEAT data on the positron fractions are an average for the results from the HEAT94 experiment flown from Fort Sumner and HEAT95 from Lynn Lake and differ somewhat from those derived from their most recent electron and positron flux values.

4.2. Interpretation of Results

Because of the large scatter of data points in Figures 9, 10, and 11 and the extent of the energy domain over which

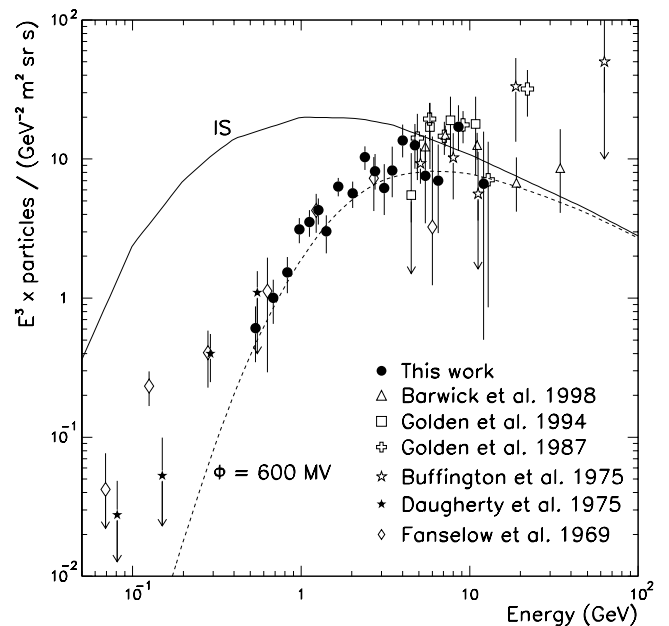


FIG. 10.—Positron spectrum multiplied by E^3 (E is the energy in GeV) measured by CAPRICE94 and other balloon-borne experiments. The solid line labeled IS is the calculated interstellar secondary positron spectrum (Moskalenko & Strong 1998). The dashed line is the same spectrum modulated according to eq. (2) with a modulation parameter $\phi = 600$ MV.

TABLE 4
POSITRON FRACTION

Energy Bin at the Spectrometer (GeV)	Mean Energy at ToA ^b (GeV)	Positron Fraction ^a $\frac{e^+}{e^+ + e^-}$
0.3–0.4	0.54	0.223 ± 0.081
0.4–0.6	0.75	0.160 ± 0.034
0.6–0.8	1.04	0.177 ± 0.025
0.8–1.1	1.40	0.144 ± 0.019
1.1–1.5	1.90	0.106 ± 0.015
1.5–2.0	2.55	0.092 ± 0.014
2.0–3.0	3.56	0.082 ± 0.015
3.0–5.0	5.61	$0.070^{+0.019}_{-0.017}$
5.0–7.0	8.58	$0.129^{+0.049}_{-0.039}$
7.0–10.0	12.11	$0.056^{+0.073}_{-0.049}$

^a The quoted errors are a combination of statistical and systematic errors.

^b Top of the Atmosphere.

the measurements were carried out during the CAPRICE94 experiment, we propose to interpret the data mainly from this experiment.

4.2.1. Electron and Positron Spectra

The solid circles and squares in Figure 12 show the electron and positron spectra measured by the CAPRICE94 experiment, and the solid curves are the recent theoretical estimates of the interstellar electron and positron spectra (*solid lines*) by Moskalenko & Strong (1998; see also Figs. 9 and 10). These calculations were based on a diffusive halo model with momentum-dependent propagation of the cosmic rays in the Galaxy. These authors (Moskalenko & Strong 1998) deduced the shape of the injection spectrum of primary electrons using the observed spectra of Galactic gamma-ray and nonthermal radio background radiation.

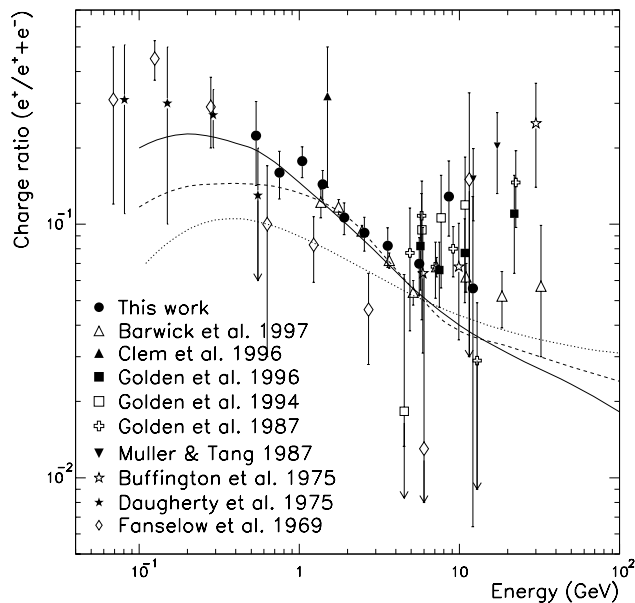


FIG. 11.—Positron fraction as a function of energy measured by CAPRICE94 and several other experiments. The dotted line is the secondary positron fraction calculated by Protheroe using the leaky-box model (Protheroe 1982). The dashed and solid lines are the secondary positron fraction calculated by Moskalenko & Strong (1998) with and without reacceleration of cosmic rays, respectively.

They found that the injection spectrum has a power-law index of -2.1 below 10 GeV that steepens to -2.4 above 10 GeV. To match the calculated spectrum with the direct measurements, they have chosen to normalize the calculated flux at 9 GeV with the measured value of 3.2×10^{-1} ($\text{GeV m}^2 \text{sr s}$)⁻¹. The positron spectrum was calculated by Moskalenko & Strong (1998) assuming that all positrons were of secondary origin and produced by the interaction of cosmic-ray nuclei with interstellar matter.

To compare these calculations with the CAPRICE94 results, the solar modulation has to be taken into account. Therefore, we have modulated the calculated interstellar spectra as described in § 4.2.3 with a modulation parameter $\phi = 600$ MV. These spectra are shown in Figure 12 (see also

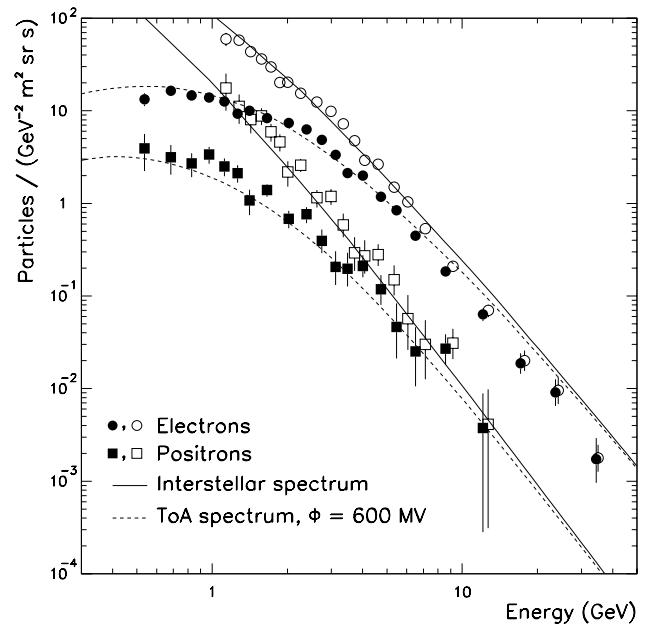


FIG. 12.—CAPRICE94 electron (*circles*) and positron (*squares*) spectra along with predictions from Moskalenko & Strong (1998). The solid symbols are the fluxes at the top of the atmosphere and the open symbols are the interstellar fluxes demodulated according to eq. (2) with modulation parameter $\phi = 600$ MV. The solid lines are the calculated interstellar electron and positron spectra using a diffusive-halo model without reacceleration of the cosmic rays, and the dashed curves are the modulated spectra.

Figs. 9 and 10) as dashed curves. The open circles and squares shown in this figure are the CAPRICE94 interstellar electron and positron fluxes, as demodulated according to equation (2), with the same modulation parameter. A satisfactory agreement is found between the modulated theoretical positron spectrum and the CAPRICE94 data. All CAPRICE94 positron data points agree within 2σ with the modulated theoretical spectrum that indicates a pure secondary nature for the positron component in the cosmic radiation. However, this conclusion depends on the solar modulation model used.

On the other hand, the CAPRICE94 electron spectrum agrees with the modulated spectrum of the theoretical curve (Moskalenko & Strong 1998) only below 6 GeV. Above 6 GeV, the theoretical spectrum is flatter than the data. In fact, the CAPRICE94 interstellar electron spectrum (*open circles* in Fig. 12) can be fitted as a power law in energy between 6 and 35 GeV with a spectral index of -3.6 ± 0.2 , which can be compared with a value of -3.16 obtained for the calculated interstellar spectrum of Moskalenko & Strong (1998) in the same energy range. It has to be said that in this energy range the “real” electron interstellar spectrum could have a more complicated spectral form because of the transition from a source spectrum to a spectrum fully steepened by radiative energy losses. This indicates that the injection spectrum is steeper than the one used by Moskalenko & Strong (1998), as suggested in Stephens (1990a). In fact, Stephens (1990a) showed that the electron data can be explained in the framework of an energy-dependent, leaky-box model without reacceleration by using a steeper injection spectrum for electrons, with an index of about -2.5 , than that for the nucleon component. The Moskalenko & Strong (1998) spectrum would agree better with CAPRICE94 high-energy fluxes if a lower normalization value for the flux was to be used. However, if this normalization is chosen to fit the CAPRICE94 high-energy data, then the low-energy interstellar CAPRICE94 electron spectrum, as shown by the open circles in Figure 12, would be steeper than the Moskalenko & Strong (1998) spectrum.

4.2.2. Positron Fraction

Figure 11 shows the CAPRICE94 positron fraction as a function of energy together with theoretical predictions. The dotted line is the calculation of the secondary positron fraction by Protheroe 1982 using the leaky-box model for Galactic propagation. It clearly differs from nearly all data both at high and low energies. This is true also if this calculation is compared with the other experimental results as discussed by Muller & Tang (1990) and Stephens (1990b).

A better agreement with the low-energy data (below 5 GeV) is obtained by the recent calculation of Moskalenko & Strong (1998). The solid and dashed lines in Figure 11 are, respectively, the results of this calculation without and with reacceleration of the cosmic rays during their propagation in the Galaxy. The solid line in this figure was obtained from the theoretical interstellar e^- and e^+ spectra shown in Figure 12. Both models fit nicely the experimental data below 5 GeV, with the model without reacceleration fitting more closely the data below 1 GeV. However, the uncertainties on the data are too large to infer any conclusion as to which of the two models is to be preferred. It is also important to notice that the theoretical positron fractions of Moskalenko & Strong (1998) are obtained using the interstellar spectra; hence, solar modulation could affect the

result. As shown in the next section, even the simple spherical model for solar modulation affects the positron fraction. The resulting calculated fraction of positrons (see Fig. 13), when modulated to the time of the CAPRICE94 flight, does not agree as well as in Figure 11. However, nearly all CAPRICE94 data points agree with the theoretical fraction within 2σ .

Even if the CAPRICE94 positron data do not extend to energies above 15 GeV, the positron fraction appears to flatten for energies higher than 5 GeV in agreement with recent measurements (Barwick et al. 1995; Golden et al. 1996; Barwick et al. 1997) but in disagreement with all theoretical predictions. This is not surprising. As can be seen in Figure 12, it is a consequence of the steeper CAPRICE94 electron spectrum compared with the calculated one. Hence, the CAPRICE94 positron fraction data also suggest a pure secondary origin of the positron component, as we concluded from the measured absolute spectrum of positrons.

4.2.3. Solar Modulation

To compare the CAPRICE94 electron and positron fluxes with theoretical calculations, it is necessary to consider the effect of the solar wind on these particles. In fact, the solar modulation affects both the species at energies less than about a few giga-electron volts.

The simplest and most widely used model for solar modulation is the spherically symmetric model in the “force-field approximation” of Gleeson & Axford (1968). In this model, the differential intensity $J(r, E, t)$ at a radial distance r from the Sun and at time t , for a total energy E of the cosmic-ray particle, is related to the time-independent

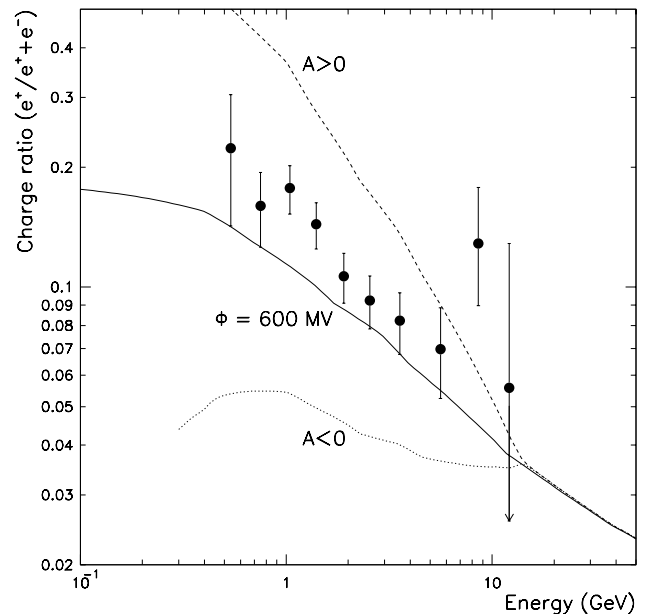


FIG. 13.—CAPRICE94 positron fraction as a function of energy. The solid line is the Moskalenko & Strong (1998) prediction for the secondary positron fraction modulated, according to eq. (2), to the solar activity of the CAPRICE94 flight ($\phi = 600$ MV). Two theoretical curves obtained by modulating the Moskalenko & Strong (1998) interstellar positron fraction with a charge-sign-dependent solar modulation (Clem et al. 1996) are shown: dashed line for positive solar polarity cycles ($A > 0$); dotted line for negative polarity cycles ($A < 0$).

interstellar intensity $J(\infty, E)$ as

$$J(r, E, t) = \frac{E^2 - E_0^2}{[E + \Phi(t)]^2 - E_0^2} J[\infty, E + \Phi(t)], \quad (2)$$

where E_0 is the rest energy (mass) of the particle and Φ a parameter that can be interpreted as the energy loss experienced by the cosmic-ray particle when approaching the Earth from infinity. Assuming that the diffusion of the particles in the magnetic field is described by a diffusion coefficient k separable with a form $k = \beta k_1(r) k_2(R)$ (β is velocity and R is rigidity of the particle), then Φ is related to the solar modulation parameter ϕ by the expression (Gleeson & Axford 1968)

$$\Phi = \frac{ZeR}{k_2(R)} \phi. \quad (3)$$

An empirical expression for $k_2(R)$ was given by Rastoin et al. (1996) with $k_2(R) = 1$ up to a breaking rigidity R_0 and $k_2(R) = R$ above it. Above R_0 , this gives $\Phi = |Z|e\phi$. Comparing electron data taken with the Ulysses spacecraft, Rastoin et al. 1996 concluded that the data was consistent with a breaking rigidity $R_0 = 0.1$ GV. This value of R_0 is well below the lowest CAPRICE94 data point; hence, we can apply this model using the solar modulation parameter alone over the entire domain of the present data. This parameter can be functionally related (see, e.g., Golden et al. 1995) to neutron monitor counter data as that from CLIMAX.⁵ The parameter ϕ for the CAPRICE94 flight using this method was found to be 500 MV. However, when comparing the measured proton and helium spectra from the same experiment, a value of 600 MV for ϕ fits the data better (see Boezio et al. 1999a); hence, we use this value of ϕ for the electron components also. The open circles and squares in Figure 12 show the CAPRICE94 interstellar electron and positron fluxes demodulated according to equation (2) with a solar modulation parameter $\phi = 600$ MV. The dashed lines in Figures 9 and 10 show the electron and positron spectra by Moskalenko & Strong (1998), which were modulated with the same solar modulation parameter.

To explain the time dependence of the electron spectrum and the positron fraction, solar-modulation models including the effect of charge sign dependence have been invoked (Moraal, Jokipii, & Mewaldt 1991; Tuska, Evenson, & Meyer 1991; Clem et al. 1996). Figure 13 has the same data points as Figure 11 but with different theoretical curves. The solid curve is obtained making use of the positron and electron spectra by Moskalenko & Strong (1998) modulated according to equation (2) with $\phi = 600$ MV. The positron fraction is affected by solar modulation even in the force-field approximation because of the different shape of the e^- and e^+ spectra. This also means that the solar modulation has to be taken into account when comparing different measured positron fractions for energies below 10 GeV. However, the two most statistically significant measurements below 10 GeV (this work and the HEAT results) can be safely compared because the data were taken in the same year.

The dashed and dotted lines are the Moskalenko & Strong (1998) interstellar positron fraction modulated

according to a model proposed by Clem et al. (1996) assuming a charge-sign-dependent solar modulation in which the dependence is estimated from experimental data. The dashed line is the positron fraction modulated for a positive solar polarity cycle ($A > 0$), while the dotted line is for negative polarity ($A < 0$). CAPRICE94 flew during a positive polarity cycle and it appears that the calculated curve is not in agreement with the measured positron fraction below 5 GeV. Between 5 and 10 GeV, the calculated positive polarity curve is in better agreement with the data. However, over the whole energy range, the Moskalenko & Strong (1998) positron fraction, modulated according to the spherically symmetric model, fits the data better than that modulated according to the charge-sign-dependent model of Clem et al. (1996). The same conclusion can be drawn from Figure 12, which indicates a similar effect of the solar modulation for both electron and positron spectra. However, this does not exclude a possible charge sign dependence for the negative polarity solar cycles as suggested by Tuska et al. (1991).

As discussed in § 4.2.1, the Moskalenko & Strong (1998) electron spectrum would agree with CAPRICE94 data at high energies if a lower normalization was used. In this case, the theoretical calculations would agree with the low-energy CAPRICE94 electron fluxes only if the electrons were less affected by solar modulation than the positively charged cosmic rays. This appears to be in contradiction with the positive solar polarity period in which CAPRICE94 data were taken. Furthermore, it is not possible to reproduce the CAPRICE94 data at all energies using a spherically symmetric model of the solar modulation on the Moskalenko & Strong (1998) electron spectrum even if the normalization is left as a free parameter.

Above 10 GeV, the solar modulation and, consequently the charge sign dependence, has too small an effect on the spectra to explain the increase or flatness of the positron fraction.

5. SUMMARY AND CONCLUSIONS

In this work, the electron and positron spectra and the positron fraction measured with the CAPRICE94 experiment have been presented.

The electron spectrum was determined over two decades in energy, from 460 MeV up to 44 GeV. The spectrum is in very good agreement with other measurements by the WIZARD collaboration and the theoretical calculation below 6 GeV by Moskalenko & Strong (1998), which assumed momentum-dependent diffusion without reacceleration as the propagation mechanism in the Galaxy. Above this energy, the CAPRICE94 electron spectrum is steeper and lower than the calculated spectrum. The difference between the observed and the calculated spectra is too large to be ascribed to experimental uncertainties. Another recent measurement (Barwick et al. 1998) disagrees with CAPRICE94 on the absolute fluxes but has a similar shape. This could indicate that the injection spectrum is steeper than the one assumed by Moskalenko & Strong (1998) as proposed by Stephens (1990a). This could be significant in terms of explaining the flattening of the positron fraction at energies above 5 GeV.

The positron spectrum was measured between 0.5 and 15 GeV. A good agreement is found with other measurements in the same energy range and with the theoretical calcu-

⁵ University of Chicago, 1996, National Science Foundation Grant ATM-9420790, http://ulysses.uchicago.edu/NeutronMonitor/neutron_mon.html.

lation of Moskalenko & Strong (1998) indicating that all positrons are of secondary origin.

The fraction of positron was also studied in the energy range from 0.5 to 15 GeV. Again, all CAPRICE94 data points are in agreement with other experimental results and, below 5 GeV, with the predicted fraction by Moskalenko & Strong (1998). Above 5 GeV, all experimental data tend to disagree with the theoretical predictions. This may be an indication of a contribution from positron sources, such as annihilations of WIMPs (e.g., Muller & Tang 1990; Coutu et al. 1997), but it can be explained with a steepening of the electron spectrum. In fact, looking at Figure 12, it is the electron flux that decreases with increasing energy with respect to the calculated one, while the positron flux agrees well with the calculation.

The solar modulation was also studied. The simple force-field approximation of the spherically symmetric model was used to modulate the Moskalenko & Strong (1998) spectra. It appears that both the e^- and the e^+ spectra agree well below 6 GeV (see Fig. 12) with the modulated theoretical spectra. This indicates that they were subjected to a similar solar modulation and that if there was a charge-sign dependence in the modulation, the effect of that should have been small during the CAPRICE94 flight. A similar conclusion

can be reached from the positron fraction, in which the calculated fraction (Moskalenko & Strong 1998) modulated according to the force-field approximation fits the CAPRICE94 data better than that modulated using the simple charge-sign-dependent model of Clem et al. (1996). However, if the normalization of the Moskalenko & Strong (1998) electron spectrum is varied to reproduce the CAPRICE94 high-energy data points, then either the low-energy interstellar spectrum derived from the CAPRICE94 data would be steeper than that determined by Moskalenko & Strong (1998) or the CAPRICE94 data would not agree with a spherically symmetric model for the solar modulation.

This work was supported by NASA Grant NAGW-110; the Istituto Nazionale di Fisica Nucleare, Italy; the Agenzia Spaziale Italiana; DARA and DFG in Germany; EU SCIENCE; the Swedish National Space Board and the Swedish Council for Planning and Coordination of Research. We wish to thank the National Scientific Balloon Facility and the NSBF launch crew that served in Lynn Lake. We would also like to acknowledge the essential support given by the CERN TA-1 group and the technical staff of NMSU and of INFN.

REFERENCES

- Aversa, F., et al. 1995, *Nucl. Instrum. Methods Phys. Res. A*, 360, 17
 Barbiellini, G., et al. 1996a, *Nucl. Instrum. Methods Phys. Res. A*, 371, 169
 ———. 1996b, *A&A*, 309, L15
 Barwick, S. W., et al. 1995, *Phys. Rev. Lett.*, 75, 390
 ———. 1997, *ApJ*, 482, L191
 ———. 1998, *ApJ*, 498, 779
 Basini, G., et al. 1995, *Proc. 24th Int. Cosmic-Ray Conf. (Rome)*, 3, 1
 Bocciolini, M., et al. 1993, *Nucl. Instrum. Methods Phys. Res. A*, 333, 77
 ———. 1996, *Nucl. Instrum. Methods Phys. Res. A*, 370, 403
 Boezio, M. 1998, Ph.D. thesis, Royal Institute of Technology, Stockholm, Sweden
 Boezio, M., et al. 1997, *ApJ*, 487, 415
 ———. 1999a, *ApJ*, 518, 457
 ———. 1999b, *Phys. Rev. Lett.*, 82, 4757
 ———. 1999c, *Proc. 26th Int. Cosmic-Ray Conf. (Salt Lake City)*, 3, 57
 Buffington, A., Orth, C. D., & Smooth, G. F. 1975, *ApJ*, 199, 669
 Carlson, P., et al. 1994, *Nucl. Instrum. Methods Phys. Res. A*, 349, 577
 Clem, J. M., et al. 1996, *ApJ*, 464, 507
 Coutu, S., et al. 1997, *Proc. 25th Int. Cosmic-Ray Conf. (Durban)*, 4, 213
 Daniel, R. R., & Stephens, S. A. 1965, *Phys. Rev. Lett.*, 15, 769
 ———. 1974, *Rev. Geophys. Space Phys.*, 12, 233
 Daugherty, J. K., et al. 1975, *ApJ*, 198, 493
 De Shong, J. A., Hildebrand, R. H., & Meyer, P. 1964, *Phys. Rev. Lett.*, 12, 3
 Earl, J. A. 1961, *Phys. Rev. Lett.*, 6, 125
 Fanselow, J. L., Hartman, R. C., Hildebrand, R. H., & Meyer, P. 1969, *ApJ*, 158, 771
 Finetti, N. 1998, Ph.D. thesis, Università degli studi, Perugia, Italy
 Gleeson, L. J., & Axford, W. I. 1968, *ApJ*, 154, 1011
 Golden, R. L., et al. 1978, *Nucl. Instrum. Methods Phys. Res.*, 148, 179
 Golden, R. L., et al. 1984, *ApJ*, 287, 622
 ———. 1987, *A&A*, 188, 145
 ———. 1991, *Nucl. Instrum. Methods Phys. Res. A*, 306, 366
 ———. 1994, *ApJ*, 436, 769
 ———. 1995, *Proc. of 24th Int. Cosmic-Ray Conf. (Rome)*, 4, 828
 ———. 1996, *ApJ*, 457, L103
 Hartman, R. C., & Pellerin, C. J. 1976, *ApJ*, 204, 927
 Hof, M., et al. 1994, *Nucl. Instrum. Methods Phys. Res. A*, 345, 561
 Lafferty, G. D., & Wyatt, T. T. 1995, *Nucl. Instrum. Methods Phys. Res. A*, 355, 541
 Meyer, P., & Vogt, R. 1961, *Phys. Rev. Lett.*, 6, 193
 Mitchell, J., et al. 1996, *Phys. Rev. Lett.*, 76, 3057
 Moraal, H., Jokipii, J. R., & Mewaldt, R. A. 1991, *ApJ*, 367, 191
 Moskalenko, I. V., & Strong, A. W. 1998, *ApJ*, 493, 694
 Müller, D., & Tang, K. K. 1987, *ApJ*, 312, 183
 ———. 1990, *Proc. 21st Int. Cosmic-Ray Conf. (Adelaide)*, 3, 249
 Piccardi, P. 1998, Ph.D. thesis, Università degli studi, Firenze, Italy
 Protheroe, R. J. 1982, *ApJ*, 254, 391
 Rastoin, C., et al. 1996, *A&A*, 307, 981
 Schmidt, P. 1972, *J. Geophys. Res.*, 77, 3295
 Shea, M. A., & Smart, D. F. 1983, *Proc. 18th Int. Cosmic-Ray Conf. (Bangalore)*, 3, 411
 Stephens, S. A. 1981, *Proc. 17th Int. Cosmic-Ray Conf. (Paris)*, 4, 282
 ———. 1990a, *Proc. 21st Int. Cosmic-Ray Conf. (Adelaide)*, 3, 241
 ———. 1990b, *Proc. 21st Int. Cosmic-Ray Conf. (Adelaide)*, 11, 99
 Sullivan, J. D. 1971, *Nucl. Instrum. Methods Phys. Res.*, 95, 5
 Tuska, E. B., Evenson, P., & Meyer, P. 1991, *ApJ*, 373, L27
 Weber, N. 1997, Ph.D. thesis, Royal Institute of Technology, Stockholm, Sweden